LETTERS

Open-to-closed transition in apo maltose-binding protein observed by paramagnetic NMR

Chun Tang[1], Charles D. Schwieters[2] & G. Marius Clore[1]

Large-scale domain rearrangements in proteins have long been recognized to have a critical function in ligand binding and recognition, catalysis and regulation[1–5]. Crystal structures have provided a static picture of the apo (usually open) and holo usually closed) states. The general question arises as to whether the apo state exists as a single species in which the closed state is energetically inaccessible and interdomain rearrangement is induced by ligand or substrate binding, or whether the predominantly open form already coexists in rapid equilibrium with a minor closed species. The maltose-binding protein (MBP), a member of the bacterial periplasmic binding protein family[6], provides a model system for investigating this problem because it has been the subject of extensive studies by crystallography[7,8], NMR[9–11] and other biophysical techniques[11–13]. Here we show that although paramagnetic relaxation enhancement (PRE) data for the sugar-bound form are consistent with the crystal structure of holo MBP, the PRE data for the apo state are indicative of a rapidly exchanging mixture (ns to μs regime) of a predominantly (~95%) open form (represented by the apo crystal structure) and a minor (~5%) partially closed species. Using ensemble simulated annealing refinement against the PRE data we are able to determine a $\langle r^{-6} \rangle$ ensemble average structure of the minor apo species and show that it is distinct from the sugar-bound state.

The PRE is proportional to the $\langle r^{-6} \rangle$ average of the distance between a proton and the paramagnetic centre. Owing to the large magnetic moment of an unpaired electron, the PRE is detectable up to large distances. In a system comprising two or more species in rapid exchange, the observed transverse PRE rate, Γ_2, is a population-weighted average of the Γ_2 rates of the component species[14,15]. As a result, the PRE is exquisitely sensitive to the presence of minor species, even as low as ~0.5–1%, provided that the distances between the paramagnetic centre and the protons of interest are much shorter in the minor species than the major one. In previous work we made use of this property of the PRE to detect transient intermediates involved in the target search process whereby a transcription factor locates its specific DNA target site[14] and to reveal semi-quantitatively the distribution of an ensemble of transient encounter complexes that facilitate stereospecific complex formation in protein–protein association[15]. Here we extend the use of the PRE to elucidate quantitatively the structure of a minor protein conformer in rapid exchange with the major conformer in the context of interdomain rearrangement. The ability to observe minor species in an equilibrium ensemble affords new insights into our understanding of weakly populated high-energy states of proteins.

MBP comprises amino-terminal and carboxy-terminal domains (NTDs and CTDs, respectively) connected by three linker segments (Fig. 1)[7,8]. Crystal structures of the apo and holo states of MBP reveal hinge-bending within the linker region that results in a ~35° rigid

body domain reorientation on the binding of sugar (Fig. 1a)[7,8]. Solution dipolar couplings (RDC) for the apo and holo (malto-triose-bound) states agree well with the respective crystal structures[10], with RDC R-factors[16] of ~14% (Supplementary Fig. 1a, b). Small-angle X-ray scattering (SAXS) data for apo MBP in solution are also consistent with the apo crystal structure (Supplementary Fig. 2a). However, the RDC and SAXS observables, unlike the PRE, are linear weighted averages of the species present in solution and are therefore insensitive to states with low populations (Supplementary Fig. 1c).

The paramagnetic probe used for PRE measurements was a nitroxide spin-label (2,2,6,6-tetramethyl-1-piperidinyloxy; TEMPO) conjugated through a maleimide group to engineered cysteine residues, D41C and S211C (one at a time), located in the NTD and CTD, respectively, at the periphery of the interface between the two domains. The D41C and S211C sites have previously been used for electron paramagnetic resonance studies[12]. The structure in the vicinity of the two mutations is the same in the apo and holo crystal structures[7,8]; NMR data indicate that these regions are rigid[10], and the spin-labels do not perturb either the backbone structure or ligand-binding characteristics (Supplementary Figs 3 and 4, respectively).

Transverse PRE rates, Γ_2, of the backbone amide protons (^1H_N) were measured for holo (matotriose-bound) and apo MBP (Fig. 2a, b for D41C; Supplementary Fig. 6 for S211C). Although the intra-domain PREs for holo and apo MBP are similar (Supplementary Fig. 7), the interdomain PREs are clearly different (Fig. 2a, b, and Supplementary Fig. 6c, d). To ascertain the agreement between observed and calculated PREs quantitatively, ensemble paramagnetic probe simulated annealing[17] was employed with a six-conformer representation (Supplementary Fig. 8) to optimize the conformational space sampled by the probe, refining either against the intradomain
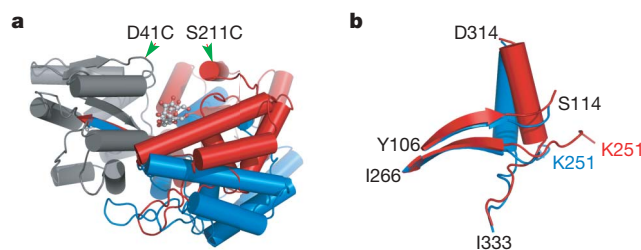

Figure 1 | Domain reorientation of MBP on binding maltotriose. a, View illustrating domain rearrangement in the crystal structures of apo (1OMP[7]) and holo (3MBP[8]) MBP. b, Close-up of the linker regions. The NTDs of apo and holo MBP are superimposed (grey); the conjugation sites (D41C and S211C) for the nitroxide spin-labels are indicated by the arrows in a, the CTDs and linker regions of apo and holo MBP are coloured in blue and red, respectively, and the maltotriose substrate is shown as balls and sticks.

[1]Laboratory of Chemical Physics, Building 5, National Institute of Diabetes and Digestive and Kidney Diseases, National Institutes of Health, Bethesda, Maryland 20892-0520, USA. [2]Division of Computational Bioscience, Building 12A, Center for Information Technology, National Institutes of Health, Bethesda, Maryland 20892-5624, USA.

PREs or against the complete PRE data sets. For both holo and apo MBP, good agreement with the intradomain PRE data are obtained (PRE Q factors[15,17], Q_{PRE}, of 0.14 and 0.20, respectively, for D41C, and 0.25 and 0.22, respectively, for S211C; Supplementary Figs 5a, b and 6a, b).

For holo MBP, refinement against the intradomain PRE data predicts the interdomain Γ_2 rates well (Fig. 2a and Supplementary Fig. 5d). Paramagnetic probe refinement against all the PRE data yields Q_{PRE} values of 0.18 for D41C (Supplementary Fig. 5f, h) and 0.34 for S211C (Supplementary Fig. 6f, h) with correlation coefficients (r) of 0.98 and 0.91, respectively. Thus, the PRE data for holo MBP are consistent with a single species that corresponds to the holo MBP crystal structure (although in this instance the PRE data would not be sensitive to the presence of a small population of open form).

For apo MBP, the PRE profile for S211C is also compatible with the crystal structure of the apo state ($Q_{PRE} = 0.23$, $r = 0.96$; Supplementary Fig. 6a, c). However, the interdomain PRE profile for apo MBP D41C is inconsistent with the apo MBP crystal structure when
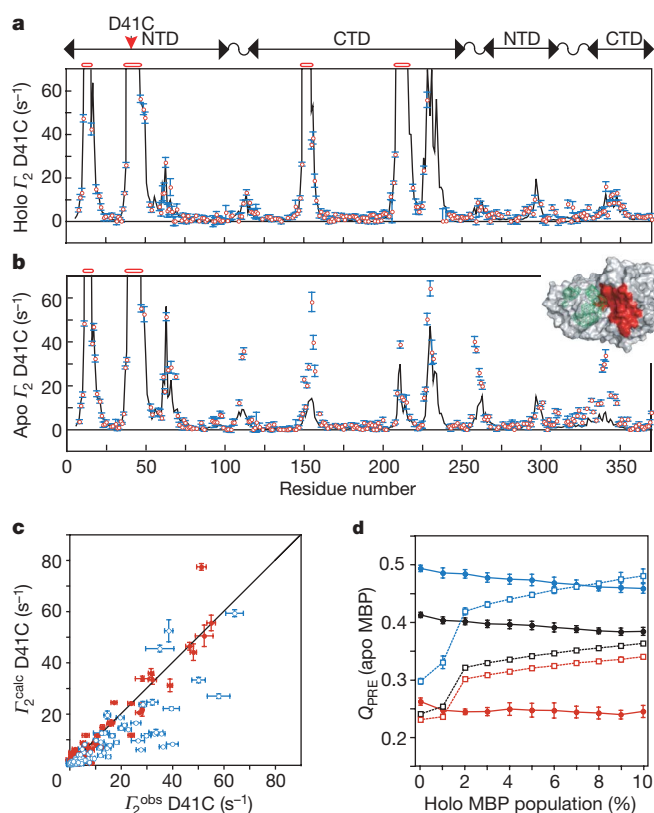
paramagnetic probe refinement is performed against either the intradomain PRE data alone (Fig. 2b and Supplementary Fig. 5a, c) or all the PRE data (Fig. 2c and Supplementary Fig. 5e, g). The discrepancies are characterized by much larger than expected interdomain experimental Γ_2 values for residues 150–157, 209–211, 226–232 and 339–348 in the CTD and residues 111–112 and 258–262 within the linker, which form a contiguous surface facing the NTD (Fig. 2b). The absence of any intermolecular PREs in a mixed sample comprising D41C nitroxide spin-labelled apo MBP at natural isotopic abundance and wild-type U-^{15}N/^{2}H-labelled apo MBP (Supplementary Fig. 9) excludes random intermolecular collisions (that is, a

Figure 2 | PRE measurements on apo and holo MBP. a, b, Comparison of observed PRE profiles (red circles) with back-calculated values (averaged from 100 independent calculations, black lines) obtained by ensemble paramagnetic probe refinement[17] against the intramolecular PRE data for holo (**a**) and apo (**b**) MBP D41C. Residues whose $^1H_N/^{15}N$ cross-peaks are completely broadened out are denoted by open red bars. The inset in **b** shows a molecular surface of apo MBP, with the conformational space sampled by the nitroxide oxygen atom bearing the unpaired electron of the spin-label represented by a green mesh and the residues with PRE discrepancies, $(\Gamma_2^{obs} - \Gamma_2^{calc}) > 10\,s^{-1}$ for apo MBP coloured in red. In the schematic diagram above **a**, the wavy lines represent linker regions. **c,** Correlation between observed and calculated PREs for apo MBP D41C obtained with probe refinement against all the observed D41C PRE data. The intradomain and interdomain PREs are shown as red and blue circles, respectively. Overall $Q = 0.41$; overall correlation coefficient, $r = 0.88$; intradomain $Q = 0.26$; intradomain $r = 0.96$; interdomain $Q = 0.49$; interdomain $r = 0.85$. **d,** Q_{PRE} for the D41C (filled circles) and S211C (open squares) apo MBP PRE data for linear combinations of apo (1OMP[7]) and holo (3MBP[8]) MBP. Overall, intradomain and interdomain PREs are shown in black, red and blue, respectively. All error bars represent 1 s.d.
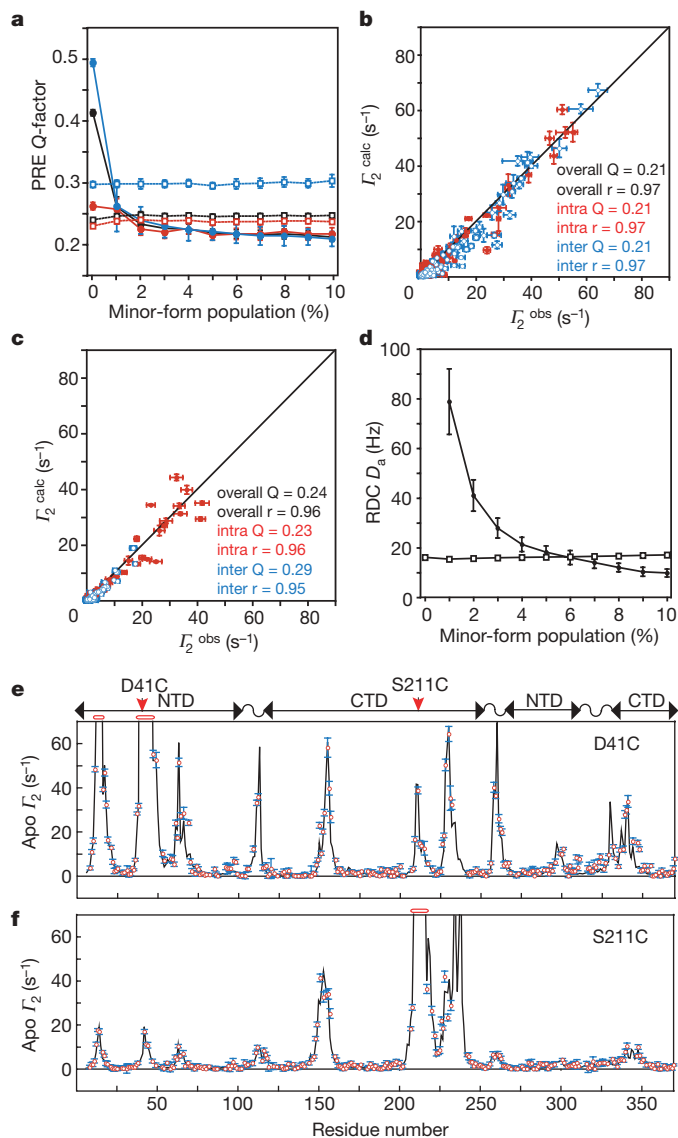
Figure 3 | Simulated annealing refinement of the minor species of apo MBP. a, Q_{PRE} as a function of minor-form population obtained by conjoined rigid-body/torsion-angle simulated annealing. Overall, intradomain and interdomain PREs are shown in black, red and blue, respectively; D41C, filled circles; S211C, open squares. Each data point is the average of 50 independent calculations. **b, c,** Correlation between observed and calculated PREs arising from D41C (**b**) and S211C (**c**) on introducing a minor species at an occupancy of 5%. **d,** Estimation of minor-species population from RDC data based on the variation of the calculated values of D_a^{NH} for the open (open squares) and minor (filled circles) forms of apo MBP obtained by SVD. The rhombicity is 0.29 ± 0.01 for the major form and 0.39 ± 0.12 for the minor form. **e, f,** Comparison of observed (red circles) and calculated (black lines) PRE profiles for D41C (**e**) and S211C (**f**) for a 5% minor species population. In the schematic diagram above **e**, the wavy lines represent linker regions. All error bars represent 1 s.d.

1079

solvent PRE) or non-specific intermolecular interactions as a source of the discrepancies.

The simplest interpretation of the apo MBP PRE data—that the relative orientation of the NTD and CTD in solution is different from that in the apo MBP crystal structure—is readily excluded. Although a single conformation can be generated by rigid-body refinement[18] that satisfies the D41C and S211C PRE data simultaneously (Supplementary Fig. 10a, b), it is inconsistent with the RDC data (Supplementary Fig. 10c). Apo MBP in solution must therefore consist of a mixture of two (or more) states in rapid equilibrium with the predominant state corresponding to the apo MBP crystal structure. The relative orientation of the NTD and CTD in the minor species is distinct from that of the holo conformation because a linear combination of apo and holo states (with paramagnetic probe refinement) results in only a minimal decrease in Q_{PRE} for D41C and a substantial increase in Q_{PRE} for S211C (Fig. 2d). The latter excludes

an occupancy of greater than 1% for the closed holo conformation, in agreement with the extrapolated population of ~0.002% derived from thermodynamic data[11].

The structure of the minor species can be resolved by conjoined rigid-body/torsion-angle simulated annealing refinement[18] in which the PRE data for both D41C and S211C are fitted simultaneously to a two-member ensemble of major (open, 1OMP[7]) and minor species. The major form is held fixed in the apo crystal structure conformation, whereas the domains of the minor species are allowed to move as rigid bodies by giving the linker residues torsional degrees of freedom (see Methods). The overall and interdomain Q_{PRE} values for D41C decrease markedly on introduction of the minor species, even at a population as low as 1%, levelling off at a population of ~5%, whereas the good agreement with the PRE data for S211C remains unaffected (Fig. 3a). At a population of 5%, the overall Q_{PRE} is 0.21 for D41C (Fig. 3b) and 0.24 for S211C (Fig. 3c).
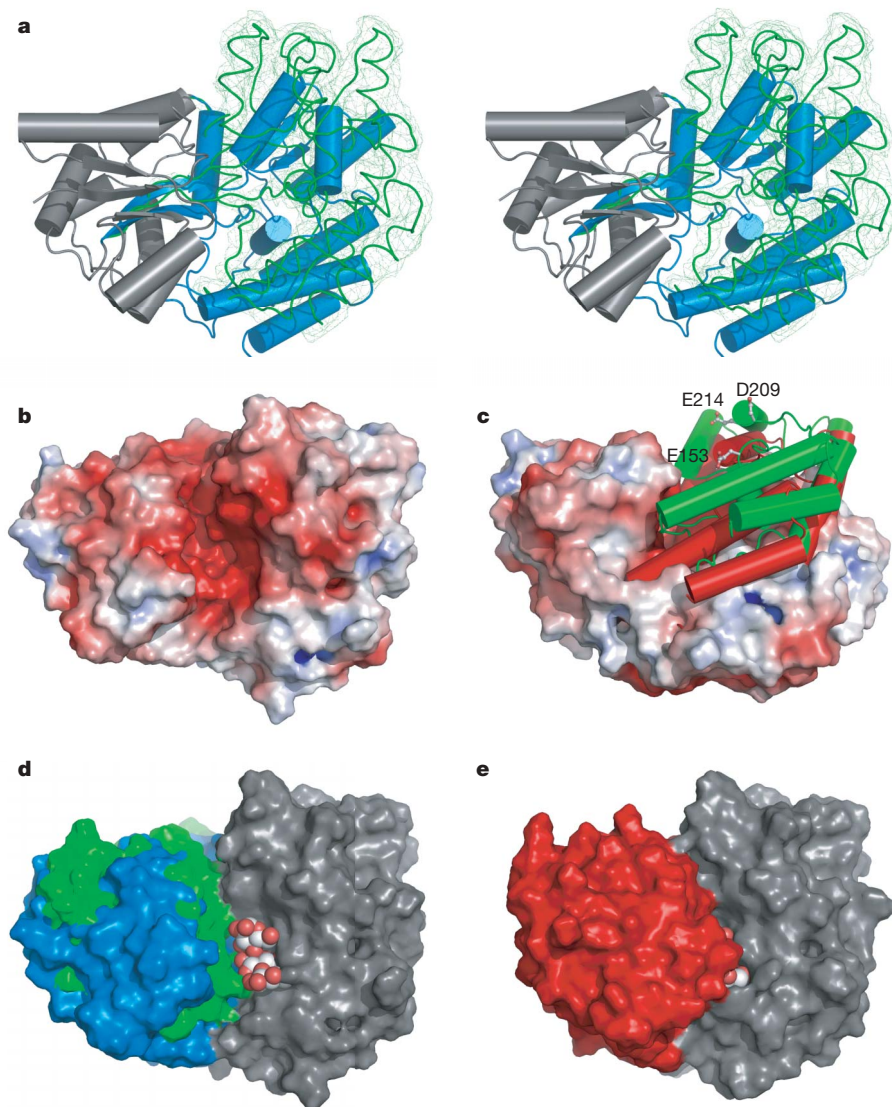

Figure 4 | Structure of the minor partly closed form of apo MBP.
a, Stereoview of the equilibrium mixture of the major open (blue cylinder) and minor closed (green smoothed backbone trace) forms of the CTD of apo MBP, with the NTDs of the two species superimposed and coloured in grey. The reweighted atomic probability map[25] for the backbone heavy atoms of the CTD in the minor form is displayed as a green mesh plotted at a threshold of 20%. **b**, Electrostatic potential surface[26] of the open form of apo MBP (1OMP[7]) drawn at ±5kT. **c**, Structural comparison of the CTD of the minor partly closed form of apo MBP (green cylinders) and holo MBP (red cylinders; 3MBP[8]), with the open form of apo MBP shown as a molecular surface colour-coded as in **b** according to electrostatic potential. **d**, Molecular surface representation of the major open and minor partly closed species of apo MBP best-fitted to the CTD (grey) with the NTD (and linker) of the major and minor species shown in blue and green, respectively. A space-filling representation of maltotriose is modelled bound to the CTD[21]. **e**, Holo MBP in the same representation as in **d**, with the NTD shown in red; the substrate is buried in holo MBP.

Further, the Q_{PRE} values for the intradomain and interdomain D41C PRE data are comparable (Fig. 3b). The overall backbone coordinate precision for the minor species is 1.3 ± 0.4 Å, the backbone precision for the CTD when best-fitting to the NTD is 3.1 ± 1.0 Å, and the uncertainty in the relative orientation of the two domains is $10.5° \pm 4.0°$ (Fig. 4a and Supplementary Fig. 11). Representing the minor species by a three-conformer ensemble results in no significant change in Q_{PRE} relative to the single-conformer representation, indicating that a single minor species is sufficient to account fully for the experimental PRE data (Supplementary Fig. 12). Structures calculated against only the D41C PRE data cross-validate against the S211C PRE data and are essentially identical to those calculated from the combined D41C and S211C PRE data (Supplementary Fig. 13). The structures also cross-validate against PRE data measured on an EDTA-Mn^{2+} derivative of apo MBP D41C (Supplementary Fig. 14).

Because the magnitude (D_a^{NH}) of the RDC alignment tensor is determined largely by shape and charge distribution[19], and because D_a^{NH} is known to be very similar for the apo and holo states aligned by phage pf1 (Supplementary Fig. 1)[10] and can therefore also be assumed to be similar for the minor apo species calculated from the PRE data, the RDC data can be used to estimate the population of the minor species by using singular-value decomposition (SVD). Although the value of D_a^{NH} and the population of the minor species cannot be determined independently because they are anticorrelated (Supplementary Fig. 15), a plot of D_a^{NH} for the open and closed forms as a function of population (Fig. 3d) indicates that at a minor species population of 5–7% the major and minor forms have comparable values of D_a^{NH} (~16 Hz). An occupancy of ~5% for the minor species is also fully consistent with the SAXS data (Supplementary Fig. 2b).

The transition between major (open) and minor forms of apo MBP involves a hinge rotation of $33.3° \pm 6.7°$, in comparison with $35.2°$ between open apo and closed holo MBP. However, the apo minor and closed holo states of MBP are not the same and are related by a domain reorientation of ~18° accompanied by a ~6-Å translation (Fig. 4c). The timescale for the transition between major and minor species of apo MBP is fast, with an upper limit of ~20 µs derived from relaxation dispersion experiments[20] and a lower limit of ~20 ns, corresponding to the rotational correlation time, from $\{^{15}N\}$-^1H heteronuclear nuclear Overhauser enhancement data (see Methods and Supplementary Information).

The interface between the NTD and CTD is lined by negatively charged residues (Fig. 4b) that are responsible for an array of hydrogen bonds with the sugar substrate in holo MBP[8]. When the substrate is removed, the energy landscape is altered and access to the holo structure is energetically highly unfavourable as a result of potential electrostatic repulsion and lack of interdomain surface complementarity within the ligand-binding cleft that cannot be offset by bridging water molecules[11]. Unfavourable interdomain interactions in the minor form of apo MBP are circumvented by translation of the CTD out of the sugar-binding pocket, exposing the negatively charged residues Glu 153, Asp 209 and Glu 214 (Fig. 4c and Supplementary Fig. 16). The distance between the carboxylate of Glu 153 in the CTD to Glu 44, Glu 45 and Asp 14 in the NTD is decreased from ~15.3, ~15.8 and ~17.1 Å, respectively, in the open apo structure to ~7.2, ~9.1 and ~9.5 Å, respectively, in the closed holo structure, but to only ~13.5, ~14.8 and ~13.8 Å, respectively, in the minor apo structure. The latter is therefore best described as a partially closed apo conformation. The sugar-binding site in the closed holo conformation is inaccessible to incoming sugars because the NTD and CTD are closely apposed and engulf the bound sugar (Fig. 4e). In the open apo state, both the NTD and CTD sugar binding surfaces are accessible to bind sugar (Fig. 4d and Supplementary Fig. 17a, c). In the partially closed apo state, the NTD sugar-binding site is partly occluded but the CTD sugar-binding site is fully exposed (Fig. 4d, and Supplementary Fig. 17a, d and Supplementary Table 1). In this

regard we note the existence of a crystal structure of a MBP–maltotetraitol complex in the fully open (apo) conformation with the ligand bound to the CTD[21].

The PRE observations reported here on apo MBP prove the existence of a long-postulated dynamic equilibrium between open and partially closed apo states, and in all likelihood reflect a general phenomenon of large-scale domain rearrangement observed in several multidomain proteins on ligand binding. The apo state exists as a rapid equilibrium of major and minor species, with the latter occupying a region of conformational space that is similar to but distinct from that occupied by the ligand-bound form. The presence of such minor species in the apo state may facilitate the transition to the holo structure that is rendered energetically accessible and stabilized by intermolecular interactions between the domains and the ligand. For MBP, the predominant fluctuations in the apo state do not involve the energetically disfavoured holo conformation and therefore the conformational change on sugar binding can be viewed as an example of induced fit.

METHODS SUMMARY

Sample preparation and NMR spectroscopy. Samples comprised 0.3 mM U-^{15}N/^{2}H-labelled MBP (D41C or S211C), which was either unmodifed (diamagnetic) or conjugated to maleimide-TEMPO (paramagnetic). ^1H_N-PRE data were acquired at 36 °C on a Bruker DRX-600 spectrometer with a cryogenic probe as described.[22] $^1D_{NH}$ RDC data were obtained by taking the difference in $^1J_{NH}$ couplings measured in aligned (~15 mg ml^{-1} phage pf1)[23] and isotropic (water) media.

Refinement and back-calculation of PREs. PREs were back-calculated by simulated annealing with Xplor-NIH[24] with the use of a six-conformer ensemble for the maleimide-TEMPO group to account for configurational space sampled owing to its flexibility[17]. Refinement of the structure of the minor form of apo MBP was performed by conjoined rigid-body/torsion-angle simulated annealing[18] subject to a target function comprising a PRE pseudopotential[17], a quartic van der Waals repulsion term to prevent atomic overlap, a multidimensional torsion-angle database potential of mean force, and appropriate torsion angle and hydrogen-bonding distance restraints within the linker. The calculated PRE for residue i of apo MBP is given by $\Gamma_{2,i}^{obs} = (1-p)\Gamma_{2,i}^{open} + p\Gamma_{2,i}^{closed}$, where p is the population of the minor species (1–10%). The minor form of apo MBP was represented by a second conformer allowing rigid-body interdomain movement by giving the linker regions (residues 106–114, 252–265 and 314–333) full torsional degrees of freedom (with the exception of the helix, residues 315–326, whose backbone was also treated as a rigid body). The structure of the predominant open form was fixed during the calculation to that of the crystal structure of apo MBP (1OMP[7]). The top 50 structures, ranked on the basis of PRE and repulsive van der Waals energies, were used for analysis. Agreement between observed and calculated PRE data are given by Q_{PRE} (Methods, equations (2) and (3))[15,17].

Full Methods and any associated references are available in the online version of the paper at www.nature.com/nature.

1. Anderson, C. M. & Zucker, F. H. Steitz, T. Space-filling models of kinase clefts and conformational change. *Science* 204, 375–380 (1979).
2. Gerstein, M., Lesk, A. M. & Chothia, C. Structural mechanisms for domain movements in proteins. *Biochemistry* 33, 6739–6749 (1994).
3. Gerstein, M. & Krebs, W. A. A database of macromolecular motions. *Nucleic Acids Res.* 26, 4280–4290 (1998).
4. Hayward, S. & Berendsen, H. J. C. Systematic analysis of domain motions in proteins from conformational change: new results on citrate synthase and T4 lysozyme. *Proteins Struct. Funct. Genet.* 30, 144–154 (1998).
5. Wolf-Watz, M. *et al.* Linkage between dynamics and catalysis in a thermophilic–mesophilic enzyme pair. *Nat. Struct. Mol. Biol.* 11, 945–949 (2004).
6. Tam, R. & Saier, M. H. Jr. Structural, functional and evolutionary relationships among extracellular solute-binding receptors of bacteria. *Microbiol. Rev.* 57, 320–346 (1993).
7. Sharff, A. J., Rodseth, L. E., Spurlino, J. C. & Quiocho, F. A. Crystallographic evidence of a large ligand-induced hinge-twist motion between the two domains of maltodextrin binding protein involved in active transport and chemotaxis. *Biochemistry* 31, 10657–10663 (1992).
8. Quiocho, F. A., Spurlino, J. C., &. Rodseth, L. E. Extensive features of tight oligosaccharide binding revealed in high-resolution structures of the maltodextrin transport/chemosensory receptor. *Structure* 5, 997–1015 (1997).

9. Skynnikov, N. R. *et al.* Orienting domains in proteins using dipolar couplings measured by liquid-state NMR: differences in solution and crystal forms of maltodextrin binding protein loaded with β-cyclodextrin. *J. Mol. Biol.* **295,** 1265–1273 (2000).
10. Evenäs, J. *et al.* Ligand-induced structural changes to maltodextrin-binding protein as studied by solution NMR spectroscopy. *J. Mol. Biol.* **309,** 961–974 (2001).
11. Millet, O., Hudson, R. P. & Kay, L. E. The energetic cost of domain reorientation in maltose-binding protein as studied by NMR and fluorescence spectroscopy. *Proc. Natl Acad. Sci. USA* **100,** 12700–12705 (2003).
12. Hall, J. A., Thorgeirsson, T. E., Liu, J., Shin, Y. K. & Nikaido, H. Two modes of ligand binding in maltose-binding protein of *Escherichia coli*: electron paramagnetic resonance study of ligand-induced global conformational changes by site-directed spin labeling. *J. Biol. Chem.* **272,** 17615–17622 (1997).
13. Zhang, Y. *et al.* Model of maltose-binding protein/chemoreceptor complex supports intrasubunit signaling mechanism. *Proc. Natl Acad. Sci. USA* **96,** 939–944 (1999).
14. Iwahara, J. & Clore, G. M. Detecting transient intermediates in macromolecular binding by paramagnetic NMR. *Nature* **440,** 1227–1230 (2006).
15. Tang, C., Iwahara, J. & Clore, G. M. Visualization of transient encounter complexes in protein-protein association. *Nature* **444,** 383–386 (2006).
16. Clore, G. M. & Garrett, D. S. *R*-factor, free *R* and complete cross-validation for dipolar coupling refinement of NMR structures. *J. Am. Chem. Soc.* **121,** 9008–9012 (1999).
17. Iwahara, J., Schwieters, C. D. & Clore, G. M. Ensemble approach for NMR structure refinement against ^{1}H paramagnetic relaxation enhancement data arising from a flexible paramagnetic group attached to a macromolecules. *J. Am. Chem. Soc.* **126,** 5879–5896 (2004).
18. Clore, G. M. & Bewley, C. A. Using conjoined rigid body/torsion angle simulated annealing to determine the relative orientation of covalently linked protein domains from dipolar couplings. *J. Magn. Reson.* **154,** 329–335 (2002).
19. Zweckstetter, M., Hummer, G. & Bax, A. Prediction of charge-induced molecular alignment of biomolecules dissolved in dilute liquid-crystalline phases. *Biophys. J.* **86,** 3444–3460 (1994).
20. Palmer, A. G. NMR characterization of the dynamics of biomacromolecules. *Chem. Rev.* **104,** 3623–3640 (2004).
21. Duan, X. & Quiocho, F. A. Structural evidence for a dominant role of nonpolar interactions in the binding of a transport/chemosensory receptor to its highly polar ligands. *Biochemistry* **41,** 706–712 (2002).
22. Iwahara, J., Tang, C. & Clore, G. M. Practical aspects of ^{1}H transverse paramagnetic relaxation enhancement measurements on macromolecules. *J. Magn. Reson.* **184,** 185–195 (2007).
23. Clore, G. M., Starich, M. R. & Gronenborn, A. M. Measurement of residual dipolar couplings of macromolecules aligned in a nematic phase of a colloidal suspension of rod-shaped viruses. *J. Am. Chem. Soc.* **120,** 10571–10572 (1998).
24. Schwieters, C. D., Kuszewski, J. & Clore, G. M. Using Xplor-NIH for NMR molecular structure determination. *Progr. NMR Spectrosc.* **48,** 47–62 (2006).
25. Schwieters, C. D. & Clore, G. M. Reweighted atomic densities to represent ensembles of NMR structures. *J. Biomol. NMR* **23,** 221–225 (2002).
26. Baker, N. A., Sept, D., Joseph, S., Holst, M. J. & McCammon, J. A. Electrostatics of nanosystems: application to microtubules and the ribosome. *Proc. Natl Acad. Sci. USA* **98,** 10037–10041 (2001).

METHODS

Sample preparation. The gene encoding MBP was subcloned from the pMAL-c2x vector (New England Biolabs) into pET11a, and U-^{15}N/^{2}H-labelled (or U-^{15}N/^{13}C/^{2}H-labelled) MBP was overexpressed in *E. coli* in minimal medium prepared in ^{2}H$_2$O with ^{15}NH$_4$Cl and ^{2}H$_7$-glucose (or ^{13}C$_6$/^{2}H$_7$-glucose) as the sole nitrogen and carbon sources, respectively, supplemented by ^{15}N/^{2}H (or ^{15}N/^{13}C/^{2}H) Isogro (Isotec). The D41C and S211C point mutations were introduced one at a time by using a QuikChange kit (Stratagene). Wild-type and Cys-mutant MBP were purified sequentially with DEAE, Superdex-75 and MonoQ columns (GE Healthcare). To remove any bound carbohydrate, the protein was denatured in 2 M guanidine hydrochloride (GuHCl) and passed through a G-50 desalting column pre-equilibrated with 2 M GuHCl[27]. The denaturant was immediately removed by desalting, thereby allowing the protein to refold. Nitroxide spin-labelling was performed by adding a roughly tenfold molar excess of 4-maleimide-TEMPO (4-maleimide-2,2,6,6-tetramethyl-piperidine-1-oxyl; Aldrich) to a solution of ~20 μM MBP Cys mutant (D41C or S211C) in 10 mM Tris-HCl pH 7.4 buffer. After incubation at 25 °C for 30 min, the reaction was quenched by the addition of 10 mM 2-mercaptoethanol. The conjugated protein was further purified on a MonoQ column, and the modification was confirmed by electrospray ionization mass spectroscopy. NMR samples comprised 0.3 mM U-^{15}N/^{2}H-labelled protein (0.3 and 0.7 mM for PRE and RDC measurements, respectively) in 10 mM Tris-HCl pH 7.4 buffer, in both the absence (apo) and presence (holo) of maltotriose (2 equivalents). All NMR measurements were performed at 37 °C with Bruker spectrometers equipped with *z*-gradient cryogenic probes. Backbone assignments were based on previously published work[10] and verified by TROSY-based[28] triple-resonance NMR spectroscopy[29] using a sample of U-[^{15}N/^{13}C/^{2}H]MBP in both the apo and holo (maltotriose-bound) states.

RDC measurements. ^{1}D$_{NH}$ RDCs were obtained by taking the difference in J_{NH} couplings in aligned (~15 mg ml^{-1} pf1 phage[23]) and isotropic (water) media[30]. J_{NH} couplings were measured from the F_1 splitting between the TROSY and semi-TROSY components of the ^{1}H$_N$/^{15}N cross-peaks acquired in an interleaved manner with a ^{1}H–^{15}N TROSY-based correlation experiment[31]. The RDC *R*-factor, which scales from 0% to 100%, is defined as

$$R_{dip} = \{\langle(D_{obs} - D_{calc})^2\rangle/(2\langle D_{random}^2\rangle)\}^{1/2} \qquad (1)$$

where D_{obs} and D_{calc} are the observed and calculated values of the RDCs, respectively, and $(2\langle D_{random}^2\rangle)^{1/2}$ is the expected root mean squared deviation if the vectors were randomly distributed. The latter is given either by $(2\langle D_{obs}^2\rangle)^{1/2}$ or exactly by $[2D_a^2(4 + 3\eta^2)/5]^{1/2}$, where D_a is the magnitude of the principal component of the alignment tensor and η is the rhombicity[16]. The latter formulation is used when a single alignment tensor is required (that is, a single structure), and the former when two alignment tensors are needed (that is, for two structures). The alignment tensor(s) and calculated RDC values were obtained by SVD in Xplor-NIH[24] by using the structure coordinates and the observed RDC values. For SVD calculations incorporating the coordinates of the major and minor forms of apo MBP, with populations $(1 - p)$ and p, respectively, the calculated RDC value for residue i is given by $D_{calc}^i = (1 - p)D_{major}^i + pD_{minor}^i$. The accession codes for the coordinates of apo and holo MBP are 1OMP[7] and 3MBP[8], respectively, and protons were added by using the HBUILD facility in Xplor-NIH[24].

PRE measurements. PRE ^{1}H$_N$-Γ_2 rates are given by the difference in R_2 relaxation rates between the paramagnetic and diamagnetic states of the protein[17]. Conjugation between the maleimide ring and the sulphur atom of a Cys residue results in two equally populated enantiomers, up and down configurations relative to the plane of the maleimide ring. R_2 rates were determined from a two-time point (2 and 6 ms) interleaved measurement using a two-dimensional ^{1}H–^{15}N transverse-relaxation optimized spectroscopy (TROSY)-based experiment, as described previously[22]. As R_2 relaxation rates were determined from the initial portion of the exponential decay, the observed R_2 rate is the average of the R_2 rates for the two enantiomers (which are expected to be very similar). Each maleimide-TEMPO adduct enantiomer was therefore represented by three conformers, and PRE ^{1}H$_N$-Γ_2 rates were back-calculated with a six-conformer (3 × 2) ensemble representing the Cys-maleimide-TEMPO group to account for the flexible linker consisting of three rotatable bonds[17]. (Note that a fourth rotatable bond between the TEMPO moiety and the maleimide group does not affect the position of the nitroxide oxygen atom bearing the unpaired electron.) Because the electron relaxation rate τ_s of the free radical is much longer than that of the protein rotational correlation time τ_r, the PRE correlation time τ_c $(= (\tau_r^{-1} + \tau_s^{-1})^{-1})$ was assumed to be the same as τ_r (18.6 ns), as reported previously[22,32]. The conformational space sampled by the six-conformer ensemble of the Cys-maleimide-TEMPO group conjugated to either D41C or S211C was optimized by simulated annealing in torsion-angle space with Xplor-NIH[24]

(100 structures calculated) to minimize the difference between observed and calculated ^{1}H$_N$-Γ_2 rates[17]. The target function also includes stereochemical terms and a quartic van der Waals repulsion term to prevent atomic overlap between maleimide-TEMPO and the protein; overlap between the members of the Cys-maleimide-TEMPO ensemble, however, is permitted because the six-member ensemble represents a distribution of states. Agreement between observed and calculated Γ_2 rates is given by the PRE *Q*-factor, Q_{PRE} (ref. 17):

$$\langle Q_{PRE}\rangle = \left[\sum_i \{\Gamma_{2,i}^{obs} - \Gamma_{2,i}^{calc}\}^2 / \sum_i (\Gamma_{2,i}^{obs})^2\right]^{1/2} \qquad (2)$$

Ensemble refinement of major and minor forms of apo MBP. Refinement against the PRE data for apo MBP was performed by conjoined rigid-body/torsion-angle refinement[18,33] with the use of Xplor-NIH[24] subject to a target function comprising a PRE pseudopotential[17], a quartic van der Waals repulsion term to prevent atomic overlap[34], a multidimensional torsion-angle database potential of mean force[35], hydrogen-bonding distance restraints to preserve the integrity of the β-sheet portion of the linker, and backbone ϕ/ψ and side-chain χ torsion angle restraints for the linker residues to keep these torsion angles within the range of values adopted in apo and holo MBP. The coordinates of the NTD (residues 1–105 and 266–313) are held fixed, the CTD (residues 115–251 and 334–370) is treated as a rigid body, and the linker segments (residues 106–114, 252–265, 314–333) are given full torsional degrees of freedom with the exception of the helix (residues 315–326), which is treated as a rigid body with side-chain torsional degrees of freedom. For calculations comprising a mixture of major and minor apo MBP, a two-member ensemble refinement is used in which the major form is held fixed in the apo crystal structure form (1OMP[7]) while the CTD of the minor species (represented as a rigid body) is allowed to move relative to the NTD by allowing the linker residues to be flexible. Calculations were also performed in which the minor form was represented not by a single structure but by an ensemble of three structures. The conformational space of the paramagnetic probe, represented by the six-conformer ensemble for Cys-maleimide-TEMPO, is simultaneously refined, and its similarity between the major and minor species is enforced by a weak non-crystallographic symmetry potential. The calculated PRE for residue i is given by $\Gamma_{2,i}^{calc} = (1 - p)\Gamma_{2,i}^{major} + p\Gamma_{2,i}^{minor}$ (ref. 15), with the minor-species population ranging from 1% to 10%. For each population, the top 50 converged structures, ranked according to the PRE and van der Waals repulsive energies, were used for further analysis. The calculated Γ_2 rates for residue i displayed in the figures in both the main text and Supplementary Information are the averages over the 50 final structures, $\langle\Gamma_{2,i}^{calc}\rangle$, and the PRE *Q*-factors reported are based on these values[15]:

$$\langle Q_{PRE}\rangle = \left[\sum_i \left\{\Gamma_{2,i}^{obs} - \langle\Gamma_{2,i}^{calc}\rangle\right\}^2 / \left(\sum_i \Gamma_{2,i}^{obs}\right)^2\right]^{1/2} \qquad (3)$$

Relaxation dispersion experiments. ^{1}H $R_{1\rho}$ relaxation dispersion experiments were conducted at a ^{1}H spectrometer frequency of 600 MHz, as described[36]. No significant decrease in transverse ^{1}H$_N$ relaxation rates were observed over ^{1}H spin lock field strengths ranging from 2 to 12 kHz (12,600–75,400 radians s^{-1}). These data indicate that the exchange rate between the major and minor forms of apo MBP is faster than ~70,000 s^{-1}. No significant decrease in {^{15}N}-^{1}H heteronuclear Overhauser effects is observed within the linker region[10], giving a lower limit of ~20 ns, corresponding to the rotational correlation time of MBP.

SAXS measurements. SAXS data were collected at the BioCAT (beam line 18-ID) of the Advanced Photon Source with the incident photons at 12 keV and a sample-to-detector distance of 242.8 cm. The 110-μl samples were loaded into a 1.5-mm diameter quartz capillary thermostatically controlled at 22 °C. The data were collected in a series of 300-ms individual frames with a total exposure time of 9 s, with the sample flowing back and forth throughout the measurement to minimize possible radiation damage. Two-dimensional images accumulated on the charge-coupled device detector were corrected for the individual pixel-counting efficiencies and dark-current rates, after which radial integrations were performed to obtain the one-dimensional scattering profiles. The scattering data collected for the empty capillary, the capillary filled with the buffer and the capillary filled with the protein solution were normalized for the incident beam intensities and the respective transmissions. No inconsistencies were found by inspection of the individual successive frames, indicating the absence of radiation damage to the sample during the measurement and permitting averaging of all acquired frames. After subtraction of the empty capillary scattering from both the sample and the buffer data, scattering of the pure solvent was subtracted from the protein solution scattering by taking into account the protein volume (calculated with partial specific volume of 0.73 cm^3 g^{-1} for the protein). The data were collected at two concentrations, 5.0 and 2.5 mg ml^{-1}, and identical profiles of the data with the lowest Q in the two

data sets were observed, indicating the absence of any interparticle interference effect. The higher-concentration data were used for the subsequent analysis because of their higher signal-to-noise ratio. The data were fitted to the respective structures by using CRYSOL (with a solvent electron density of $0.3340 \, e \, \text{Å}^{-3}$)[37].

Structure analysis. Structures were displayed in PyMol[38], and electrostatic potentials were calculated with APBS[26].

27. Ganesh, C., Shah, A. N., Swaminathan, C. P., Surolia, A. & Varadarajan, R. Thermodynamic characterization of the reversible, two-state unfolding of maltose binding protein, a large two-domain protein. *Biochemistry* **36**, 5020–5028 (1997).
28. Peruvshin, K., Riek, R., Wider, G. & Wüthrich, K. Attenuated T_2 relaxation by mutual cancellation of dipole–dipole coupling and chemical shift anisotropy indicates an avenue to NMR structures of very large biologial macromolecules in solution. *Proc. Natl Acad. Sci. USA* **94**, 12366–12371 (1997).
29. Yang, D. & Kay, L. E. TROSY triple-resonance four-dimensional NMR spectroscopy of a 46 ns tumbling protein. *J. Am. Chem. Soc.* **121**, 2571–2575 (1999).
30. Bax, A., Kontaxis, G. & Tjandra, N. Dipolar couplings in macromolecular structure determination. *Methods Enzymol.* **339**, 127–174 (2001).
31. Kontaxis, G., Clore, G. M. & Bax, A. Evaluation of cross-relaxation effects and measurement of one-bond couplings in proteins with short transverse relaxation times. *J. Magn. Reson.* **143**, 184–196 (2000).
32. Hwang, P. M., Skrynnikov, N. R. & Kay, L. E. Domain orientation in β-cyclodextrin-loaded maltose binding protein: diffusion anisotropy measurements confirm the results of a dipolar coupling study. *J. Biomol. NMR* **20**, 83–88 (2001).
33. Schwieters, C. D. & Clore, G. M. Internal coordinates for molecular dynamics and minimization in structure determination and refinement. *J. Magn. Reson.* **152**, 288–302 (2001).
34. Nilges, M., Gronenborn, A. M., Brünger, A. T. & Clore, G. M. Determination of three-dimensional structures of proteins by simulated annealing with interproton distance restraints: application to crambin, potato carboxypeptidase inhibitor and barley serine proteinase inhibitor 2. *Protein Eng.* **2**, 27–38 (1988).
35. Clore, G. M. & Kuszewski, J. χ_1 rotamer populations and angles of mobile surface side chains are accurately predicted by a torsion angle database potential of mean force. *J. Am. Chem. Soc.* **124**, 2866–2867 (2002).
36. Suh, J.-Y., Iwahara, J. & Clore, G. M. Intramolecular domain–domain association/dissociation and phosphoryl transfer in the mannitol transporter of *Escherichia coli* are not coupled. *Proc. Natl Acad. Sci. USA* **104**, 3153–3158 (2007).
37. Svergun, D., Barberato, C. & Koch, M. H. J. CRYSOL: a program to evaluate X-ray scattering of biological macromolecules from atomic coordinates. *J. Appl. Cryst.* **28**, 768–773 (1995).
38. DeLano, W. L. *The PyMol Molecular Graphics System*, ⟨http://www.pymol.org⟩ (DeLano Scientific, San Carlos, CA, 2002).